Enhanced photocatalytic H_2-production activity of anatase TiO_2 nanosheet by selectively depositing dual-cocatalysts on {101} and {001} facets

Aiyun Meng [a], Jun Zhang [a,b], Difa Xu [b], Bei Cheng [a], Jiaguo Yu [a,c,*]

[a] State Key Laboratory of Advanced Technology for Material Synthesis and Processing, Wuhan University of Technology, Luoshi Road 122#, Wuhan 430070, PR China
[b] Hunan Key Laboratory of Applied Environment Photocatalysis, Changsha University, Changsha, 410022, PR China
[c] Department of Physics, Faculty of Science, King Abdulaziz University, Jeddah 21589, Saudi Arabia

ARTICLE INFO

ABSTRACT

The photocatalytic hydrogen production using solar energy through water splitting has received great attention due to the increasingly serious energy crisis. Herein, we report the controlled preparation of anatase TiO_2 nanosheet photocatalyst by selectively depositing Co_3O_4 nanoparticles (NPs) as water oxidation cocatalyst (WOC) and Pt NPs as water reduction cocatalyst (WRC) on {001} and {101} facets, respectively, using a two-step photodeposition method. The prepared TiO_2-Co_3O_4-Pt composite photocatalyst exhibits a greatly enhanced photocatalytic H_2-production activity at the optimal weight percentage of Co_3O_4 and Pt (both 1.0 wt%), exceeding that of TiO_2 nanosheet deposited with single Co_3O_4 or Pt cocatalyst by 9.4 and 1.8 times, respectively. The enhanced H_2-production activity is due to the synergetic effect of surface heterojunction between {001} and {101} facets and selective deposition of Co_3O_4 and Pt dual-cocatalysts at {001} and {101} facets, respectively. The former is beneficial for the transfer and separation of charge carriers, the latter can reduce the recombination rate of photogenerated electrons and holes and also catalyze the redox reactions. This work will provide a new route for the rational design and fabrication of highly efficient photocatalysts with dual-cocatalysts through selective surface deposition.

© 2016 Elsevier B.V. All rights reserved.

1. Introduction

With increasing environmental crisis and energy demand, photocatalytic hydrogen production from water splitting via semiconductor photocatalysts has become a promising approach to produce economical and environmentally friendly hydrogen energy by utilizing abundant water resources and sustainable solar energy [1–5]. For now, various active photocatalysts have been developed. Among them, titanium dioxide has received a lot of attention owing to its nontoxicity, chemical stability, rich source and excellent performance [6–11]. However, the further application of TiO_2 is restricted due to the rapid recombination of photogenerated electron-hole pairs, thus numerous methods have been explored to solve this problem such as doping cations or anions, coupling with other semiconductors and depositing noble metals on the surface [12–16]. Moreover, since the pioneering work by Yang et al. [17] reported the synthesis of anatase TiO_2 single crystal microsheets with highly energetic (001) facet exposed, there is an enormous interest in controlling TiO_2 crystal facets due to their fascinating shape-dependent physicochemical properties. So far, TiO_2 with different exposed facets such as {001}, {010}, {101} and {110} have been successfully obtained [18]. Among them, high quality anatase crystals with {001} facets have been most intensively studied due to its high surface energy (0.90 J m^{-2}) [19–25]. Indeed, most studies on photocatalytic decomposition of organic pollutants showed that the activities of the prepared anatase nanocrystals increase with increasing the percentage of {001} facet exposed [18,26]. However, several subsequent studies showed that anatase TiO_2 nanosheets with higher ratio of {001} to {101} (the thermodynamically stable facet with surface energy of 0.44 J m^{-2}) facets do not always exhibit higher activities especially in photocatalytic hydrogen production or CO_2 reduction [27–32]. For example, our previous work showed that the ratio

of the exposed {001} to {101} facets has a significant effect on the photocatalytic CO_2 reduction activity of anatase TiO_2, and an optimal ratio of {001} to {101} facets was observed to be about 58% to 42%. Further, the {101} and {001} facets of anatase TiO_2 exhibit different band structures and band edge positions based on the density functional theory (DFT) calculation. Thus, the exposed {101} and {001} facets can form a surface heterojunction, which is beneficial for the transfer of photoinduced electrons and holes to {101} and {001} facets, respectively, resulting in the enhancement of photocatalytic CO_2 reduction activity [31].

On the other hand, cocatalysts have been proved to play a significant role in improving both the activity and stability of photocatalysts for water splitting [33–37]. To date, numerous effective cocatalysts including water reduction cocatalyst (WRC) (such as Pt, NiO, Cu(OH)$_2$, MoS$_2$, graphene et al.) and water oxidation cocatalyst (WOC) (such as IrO$_2$, RuO$_2$, CoOx, MnOx et al.) have been developed for many semiconductor-based photocatalytic H_2-production systems [34,38,39]. And the co-loading of both WRC and WOC on the same semiconductor has been demonstrated as a successful way to further improve the photocatalytic water splitting activity compared with the loading of either a WRC or WOC alone [40–44]. However, it should be noted that the advantages of co-loading both WRC and WOC cocatalysts on the photocatalysts surface could not be fully demonstrated because these cocatalysts are randomly deposited. To resolve this problem, Liu et al. reported a SiO$_2$-Ta$_3$N$_5$ core-shell photocatalyst loaded with Pt on the inner Ta$_3$N$_5$ shell surface as WRC and IrO$_2$ on the outer shell surface as WOC, thus, the spatially separated cocatalysts promote the separation of photogenerated electrons and holes toward inner and outer surface, respectively, resulting in high photocatalytic water splitting activity [45]. Li et al. reported the selective deposition of Pt and MnOx or Co$_3$O$_4$ onto the different facets of BiVO$_4$, which also exhibited enhanced photocatalytic activity for water oxidation and dye degradation [46]. Although several successful and reliable models utilizing the co-loading method have been reported, it is still a great challenge to carefully control the deposition of the cocatalysts on different facets of photocatalysts.

Herein, we for the first time report the synthesis of anatase TiO_2 single crystal nanosheets co-deposited with Pt WRC on {101} and Co$_3$O$_4$ WOC on {001} facets, respectively, through a two-step photodeposition method. In this case, the photo-generated electrons and holes can be respectively transferred onto {101} and {001} facets due to the presence of surface heterojunction. Furthermore, the deposited Pt and Co$_3$O$_4$ dual cocatalysts can respectively capture photogenerated electrons and holes and act as reduction and oxidation active sites, leading to high photocatalytic H_2-production activity.

2. Experimental

2.1. Preparation

All reagents in this study are of analytic-grade and were used without further treatment. Anatase TiO_2 nanosheet was prepared according to our previously reported method [31]. In a typical preparation, concentrated HF solution (9 mL, ca. 40 wt%) was directly added into tetrabutyl titanate (50 mL), followed by magnetic stirring for 30 min. After that, the mixed solution was transferred to a 100 mL Teflon-lined autoclave and hydrothermally treated for 24 h at 180 °C. Finally, the white precipitation was collected, washed with distilled water and absolute ethanol for three times, and then dried at 80 °C overnight. The obtained TiO_2 nanosheet sample was further calcined at 550 °C for 2 h in a muffle furnace to remove the adsorbed F^- ions on TiO_2 surface, and labelled as T.

Photocatalyic activity experiments indicated that the TiO_2-Co$_3$O$_4$ and TiO_2-Pt composite photocatalysts respectively exhibit the highest H_2-production rate when TiO_2 couples with 1 wt% Co$_3$O$_4$ or 1 wt% Pt single cocatalyst. Thus, 1 wt% Co$_3$O$_4$ and 1 wt% Pt were chosen for the fabrication of TiO_2-Co$_3$O$_4$-Pt composite sample. Typically, the TiO_2-Co$_3$O$_4$ composite sample was prepared by photodeposition method using Co(NO$_3$)$_2$ as the precursor. 0.5 g of the above prepared TiO_2 nanosheet powder was suspended in 80 mL of NaIO$_3$ solution (0.01 M), after that, a certain amount of Co(NO$_3$)$_2$ solution (5 g L^{-1}) were added into the suspension, followed by irradiation (300 W, Xe arc lamp) under continuous stirring for 3 h. Then the suspension was filtered, washed with distilled water, and finally dried at 80 °C overnight and labelled as TC. The nominal weight percentages of Co$_3$O$_4$ to TiO_2 were 0, 0.5, 1 and 3, and the resulting samples were labelled as T, TC0.5, TC1 and TC3, respectively. The TiO_2-Co$_3$O$_4$-Pt composite sample was further prepared through the photodeposition method using H$_2$PtCl$_6$ solution as Pt source. 0.05 g of the as-prepared TC1 sample (1 wt% Co$_3$O$_4$) was suspended in methanol (20 mL) and water (60 mL) mixed solution, after that H$_2$PtCl$_6$ solution (0.13 mL, 10 g L^{-1}) was added into the suspension under continuous magnetic stirring, followed by irradiation (300 W, Xe arc lamp) for 0.5 h. Then the suspension was filtered, washed with distilled water, and finally dried at 80 °C overnight. The obtained sample was labelled as TCP. The TiO_2-Pt composite samples were also prepared using the above described method and pure TiO_2 nanosheet powder as support and labelled as TP. The nominal weight percentages of Pt to TiO_2 were 0, 0.5, 1 and 2, and the obtained samples were labelled as T, TP0.5, TP1 and TP2, respectively. Moreover, for comparison, TCP(r) sample were also prepared using TC1 and H$_2$PtCl$_6$ solution as precursors and the Pt cocatalyst was randomly deposited on the surface of TC1 through NaBH$_4$ reduction method. TC(r)P sample were also prepared utilizing TP1 (1 wt% Pt) and Co(NO$_3$)$_2$ solution as precursors using a typical impregnation method followed by post-calcination at 350 °C for 1 h.

2.2. Characterization

Powder X-ray diffraction (XRD) measurements were conducted on an X-ray diffractometer (Rigaku, Japan) using Cu Kα irradiation (λ = 0.15418 nm). Morphological observations were done on a JSM-7500 field emission scanning electron microscope (FESEM, JEOL, Japan) equipped with an X-Max 50 energy-dispersive X-ray spectroscopy (EDS, Oxford Instruments, Britain). Transmission electron microscopy (TEM) analysis was performed using a Titan G2 60-300 microscope at an accelerating voltage of 300 kV. UV–vis diffuse reflectance spectra were obtained with a UV–vis spectrophotometer (UV-2600, Shimadzu, Japan) using BaSO$_4$ powder as a reflectance standard. The Brunauer-Emmett-Teller (BET) specific surface area (S_{BET}) of the powders was analysed by nitrogen adsorption using a Micromeritics ASAP 2020 nitrogen adsorption apparatus (USA). All samples were degassed at 150 °C. The X-ray photoelectron spectroscopy (XPS) measurements were performed by a Thermo ESCALA 250, using Al Kα (1486.6 eV) irradiation (operated at 150 W) in the constant analyzer energy mode with a 30 eV pass energy. The photoelectrochemical measurement was performed in 0.5 M Na$_2$SO$_4$ solution by a CHI660C electrochemical analyzer (CHI, China) using a standard three-electrode system. The sample was coated onto a 2 × 1.5 cm FTO glass electrode, and then annealed at 450 °C for 30 min, which was used as working electrode. Pt wire and Ag/AgCl (saturated KCl) were served as counter-electrode and reference electrode, respectively. A 3 W UV-LED (365 nm) was used as the light source.

2.3. Photocatalytic hydrogen production activity

The photocatalytic H_2-production experiments were carried out in a 100 mL Pyrex flask at room temperature and atmospheric pressure, and the flask was sealed with silicone rubber septum. A 300 W Xe arc lamp (Changzhou Siyu Science Co. Ltd, China), fixed at 20 cm far away from the photocatalytic reactor, was used as light source. The focused intensity on the flask was ca. 130 mW/cm^{-2}. In a typical H_2-generated experiment, 50 mg of catalyst was added into 80 mL methanol aqueous solution (containing 25% methanol in volume). Prior to irradiation, the suspensions were bubbled with N_2 for 30 min to remove the dissolved oxygen and to form anaerobic conditions. Continuous stirring was required during whole photocatalytic reaction. 0.4 mL gas was collected intermittently from the reactor through the septum, and the produced hydrogen was detected by a gas chromatograph (GC-14C, Shimadzu, Japan, TCD, nitrogen as a carrier gas and 5 Å molecular sieve column). The apparent quantum efficiency (QE) was measured under similar photocatalytic reaction condition except that four 365 nm-LEDs (3 W, Shenzhen LAMPLIC Science Co. Ltd., China) were used as light sources instead of the Xe arc lamp.

3. Results and discussion

3.1. Phase structure and morphology

Anatase TiO_2 nanosheets were prepared by hydrothermal method and labelled as T. The samples TC1, TP1 and TCP represent TiO_2 nanosheets respectively photodeposited with 1 wt% Co_3O_4,

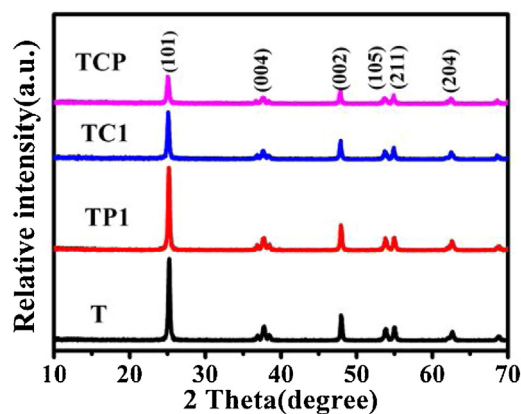**Fig. 1.** XRD patterns of T, TC1, TP1 and TCP samples.

1 wt% Pt, and 1 wt% Co_3O_4 and 1 wt% Pt (see Experimental). XRD was used to investigate the phase structure and crystallization of the prepared samples. Fig. 1 shows a comparison of the XRD patterns of different samples. As can be seen, all of the diffraction peaks at 25°, 38°, 48°, 54°, 55° and 63° can be assigned to the (101), (004), (002), (105), (211) and (204) crystal faces of anatase TiO_2 (JCPDS, No. 21-1272), respectively. No diffraction peaks of Co_3O_4 and Pt were observed in TC1, TP1 and TCP samples due to their low amount, weak crystallization and high dispersion [47]. In addition, the peak intensities decreased after the deposition of Co_3O_4 or Pt cocatalysts. This is because incident and diffracted X-ray are
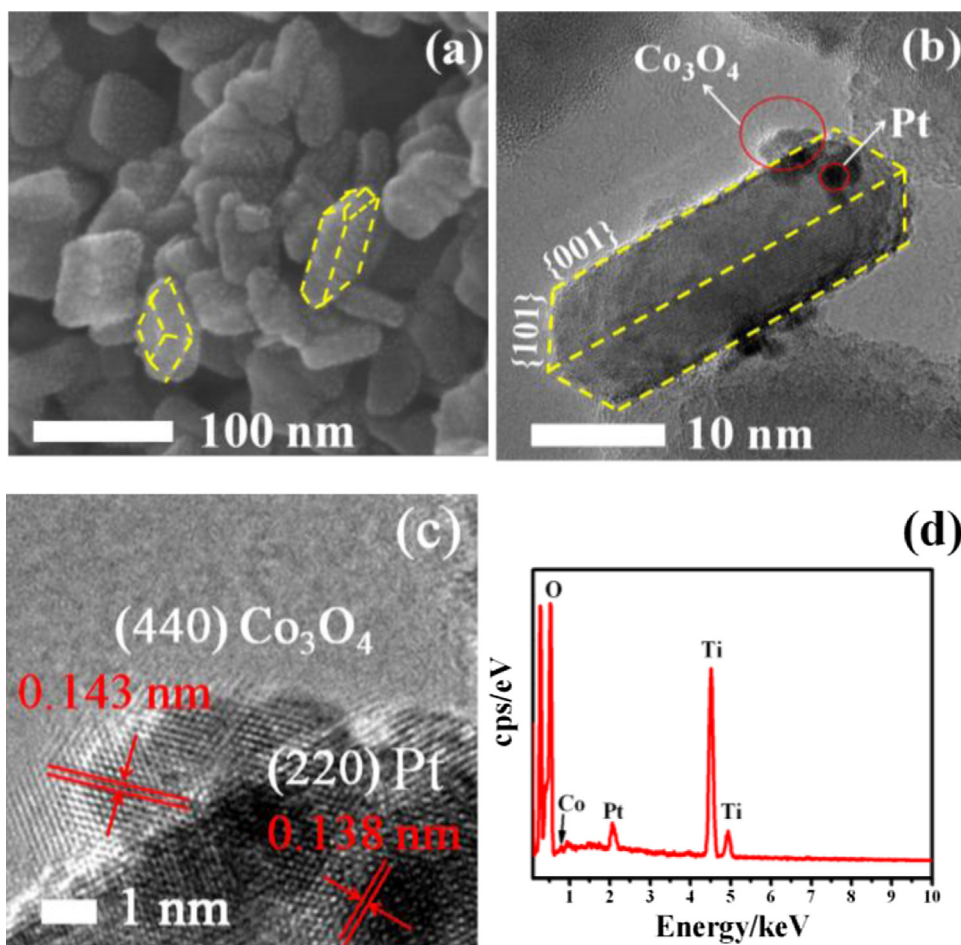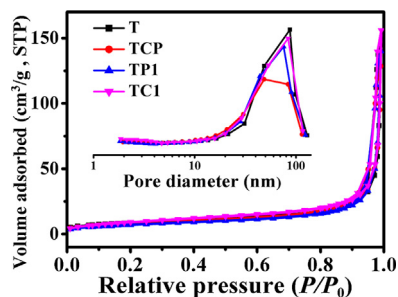

Fig. 2. FESEM (a), TEM (b), HRTEM (c) images, and EDS pattern (d) of TCP sample.

Fig. 3. Nitrogen adsorption-desorption isotherms and the corresponding pore-size distribution curves (inset) of T, TC1, TP1 and TCP samples.

Fig. 4. UV–vis diffuse reflection spectra of T, TC1, TP1 and TCP samples.

Table 1
Comparison of the specific surface areas, pore volumes, average pore sizes and activities of the samples.

Sample	$S_{BET}(m^2 g^{-1})$	Pore volume $(cm^3 g^{-1})$	Average pore size (nm)	Activity $(\mu mol\, h^{-1})$
T	31	0.07	8.90	0
TC1	35	0.08	9.50	28
TP1	27	0.08	11.5	146
TCP	29	0.08	10.6	264

weakened because of the presence of Co_3O_4 NPs and Pt NPs on the surface of TiO_2 due to their shield effect. This also further confirmed that Co_3O_4 NPs and Pt NPs were indeed deposited on the surface of anatase TiO_2 nanosheets by photodepositon method.

Fig. 2a shows the SEM image of TCP, in which TCP is a sheet-shaped structure with an average side length of ca. 80 nm and thickness of ca. 30 nm. It was confirmed by our previous work that the as-prepared TiO_2 nanosheets were composed of {101} and {001} facets [31]. The TEM image (Fig. 2b) exhibits these two facets clearly, besides, it can be seen that some small black NPs are deposited on the surface of anatase TiO_2 nanosheets. The lattice fringes of NPs on {001} and {101} facets can be observed in the enlarged high-resolution TEM image (Fig. 2c), the lattice spacing of ca. 0.143 nm can be assigned to the (440) plane of Co_3O_4 (JCPDS, No. 42-1467), and the lattice spacing of ca. 0.138 nm can be indexed to the (220) plane of Pt (JCPDS, No. 04-0802). The Pt NPs on {101} facets are darker due to its large atomic number and high electron density. Therefore, it can be concluded that Pt and Co_3O_4 NPs are selectively deposited on the {101} and {001} facets, respectively. Moreover, the intimate contact between these NPs and TiO_2 nanosheets could favor the vectorial transfer of photo-generated charge carriers, thus enhancing the charge separation and the photocatalytic activity. The EDS spectrum (Fig. 2d) further confirms that the TCP sample consists of Ti, O, Co and Pt elements.

3.2. BET surface area and pore size distributions

Fig. 3 shows the nitrogen adsorption-desorption isotherms and corresponding pore-size distribution curves of the samples. According to IUPAC (International Union of Pure and Applied Chemistry) classification, the nitrogen adsorption-desorption isotherms of all samples can be categorized as type IV, indicating the presence of mesopores [48]. The shapes of hysteresis loops are of type H3, reflecting the existence of slit-like mesopores due to the stacking of anatase TiO_2 nanosheets, which is in line with the TEM results. The corresponding pore-size distribution curves (inset in Fig. 3) show wide pore-size distribution from 2 to 100 nm, further indicating the formation of mesopores and macropores. Table 1 shows the comparison of the specific surface areas, pore volumes, average pore sizes and activities of the prepared samples. The BET surface areas decrease with the deposition of Pt NPs. It is easy to
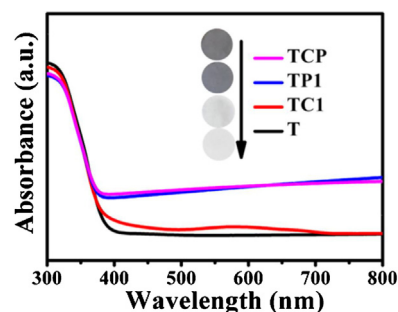
understand because the specific surface area (m^2/g) is expressed per gram of the sample. The densities of anatase TiO_2 and Pt are 3.84 and 21.45 g/cm^3, respectively [19]. So, the densities of TP and TCP samples increase due to the deposition of Pt NPs, resulting in the decrease of the BET surface areas. However, the average pore sizes of TC, TP and TCP samples increase comparing with that of pure anatase TiO_2 nanosheets. This is because TiO_2 nanosheets get thicker after the deposition of Pt NPs and Co_3O_4 NPs, forming larger slitlike pores.

3.3. UV–vis spectra

The UV–vis diffuse reflection spectra of the composite samples (Fig. 4) show no absorption edge shift compared to the pristine TiO_2, indicating that neither Co nor Pt is incorporated into the lattice of TiO_2, Co_3O_4 and Pt are only deposited on the surface of TiO_2 nanosheets. In addition, the absorption of sample TC1 in the wavelength range of 400–700 nm is slightly enhanced due to Co(II) d-d transition [49]. Moreover, for sample TP1 and TCP, an enhanced absorption in the visible light region is consistent with the dark gray color due to the deposition of Pt NPs.

3.4. XPS spectra

To probe the surface chemical composition and elemental chemical states, XPS spectra of samples were recorded. The XPS survey spectrum of sample TCP (Fig. 5a) clearly shows the peaks of Ti 2p, O 1s and C 1s. As illustrated in Co 2p high-resolution spectrum (Fig. 5b), two main peaks located at about 780.0 and 795.1 eV can be respectively ascribed to both Co $2p_{3/2}$ and Co $2p_{1/2}$. And two peaks at 785.5 and 800.6 eV are the satellite peaks of both Co $2p_{3/2}$ and Co $2p_{1/2}$, respectively [46,50]. It is reported that the spin–orbit splitting value for the mixed-valence Co_3O_4 is 15.1–15.3 eV [51]. Here, the spin–orbit splitting value of Co 2p is 15.1 eV, thus it can be concluded that the cobalt species on sample TCP should be Co_3O_4. Moreover, as shown in Fig. 5b, the Co 2p spectrum can be fitted to Co^{2+} and Co^{3+} according to the fact that the Co $2p_{3/2}$ binding energies of Co^{2+} and Co^{3+} are at 781.5 ± 0.2 and 779.6 ± 0.1 eV, respectively [51]. The existence of Co^{3+} obviously suggests that Co^{2+} is partially oxidized to Co^{3+} and the Co_3O_4 cocatalyst was successfully deposited on {001} facets of TiO_2. Fig. 5c shows the Pt 4f high-resolution spectrum. The Pt $4f_{7/2}$ and Pt $4f_{5/2}$ peaks at about 70.4 eV and 73.7 eV are assigned to metallic Pt^0. It is known that the Pt $4f_{7/2}$ binding energy of Pt^0 is around 71.2 eV. The negative shift can be attributed to the electron transfer from TiO_2 to Pt caused by strong metal-support interactions (SMSI) [52,53]. This is easy to understand because the work function (Φ) of Pt is 5.65 eV [54] versus E_{vacuum}, which can be converted into 1.1 eV versus NHE. Furthermore, the conduction band (CB) of TiO_2 (-0.26 eV versus NHE) [55] is more negative than Fermi level of Pt, thus resulting in the
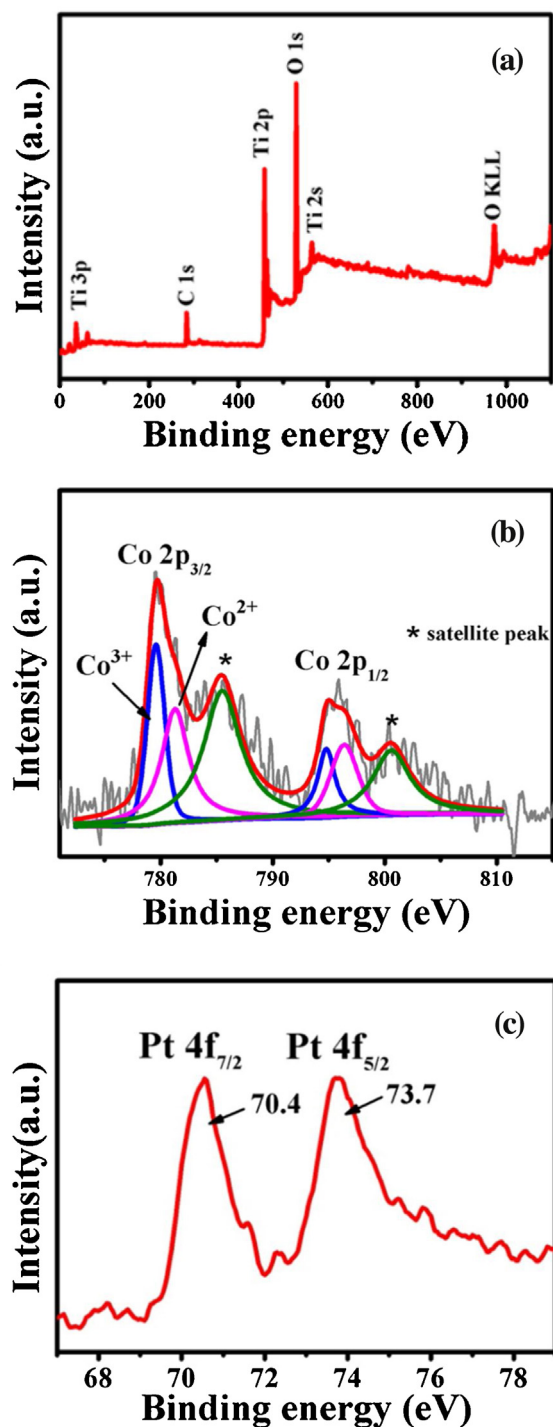
Fig. 5. XPS spectra of TCP sample. Survey (a), high-resolution XPS spectra of Co 2p (b) and Pt 4f (c).

electron migration from TiO_2 to Pt. XPS results also indicate that there is an intimate contact between Pt NPs and TiO_2 nanosheets.

3.5. Photocatalytic activity and stability

The photocatalytic hydrogen production activities were investigated in a methanol aqueous solution under 300 W xenon arc lamp irradiation. Control experiments indicate that no appreciable H_2 production is detected in the absence of either irradiation or photocatalyst, suggesting that hydrogen is produced by a photocatalytic reaction of the photocatalyst. Fig. 6 shows comparison
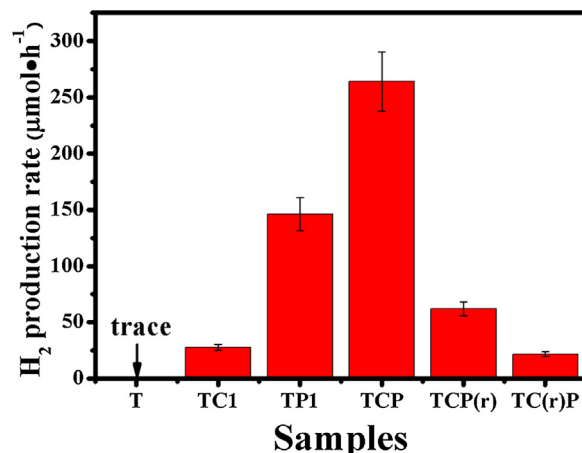

Fig. 6. Comparison of the photocatalytic H_2-production rate of T, TC1, TP1, TCP, TCP(r) and TC(r)P samples.
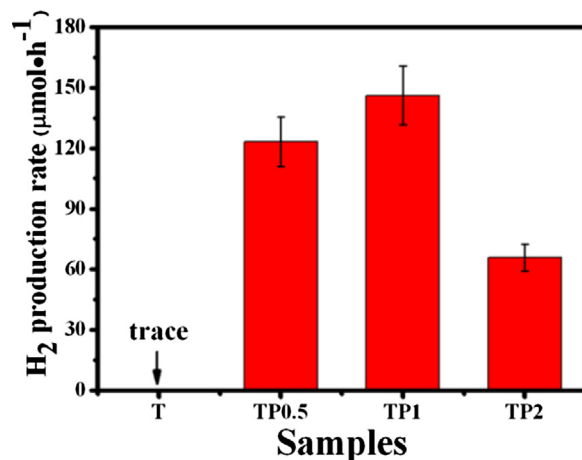

Fig. 7. Comparison of the photocatalytic H_2-production activities for TiO_2 and Pt composite samples TPx.

of the photocatalytic H_2-production rates of the samples T, TC1, TP1 and TCP. Obviously, the pristine TiO_2 shows negligible photocatalytic H_2-production activity due to the rapid recombination of photogenerated electrons and holes [55]. The low photocatalytic H_2-production activity of TiO_2 could be remarkably enhanced after loading Pt WRC or Co_3O_4 WOC, respectively (as shown in Figs. 7 and 8). It should be noted that a suitable content of Pt or Co_3O_4 cocatalyst is crucial for improving the photocatalytic activity of the photocatalysts [56]. It is well-known that due to the large work function and low overpotential for H_2 evolution, Pt is the most effective WRC in many photocatalytic water splitting systems [33]. Thus, it is not surprising that with the deposition of a suitable amount of Pt NPs (1 wt%) on {101} facets of TiO_2, the H_2-production activity could be greatly enhanced (Fig. 7). Furthermore, as an effective WOC, Co_3O_4 has been widely used as cocatalyst for enhancing photocatalytic (or photoelectrochemical) O_2 production [57,58] and H_2 production [59,60]. It is usually believed that the surface deposited Co_3O_4 NPs could be beneficial to assemble the holes and catalyse water oxidation [60,61]. Consequently, the recombination rate of electron-hole pairs will be reduced, thus leading to an enhanced H_2-production activity. In addition, with increasing the Co_3O_4 content (Fig. 8), the H_2-production activity of TiO_2-Co_3O_4 samples increases and achieves a maximum rate of 28 μmol h^{-1} when the Co_3O_4 content is 1 wt%. However, further increasing the content of Co_3O_4, the activity decreases because the excess Co_3O_4
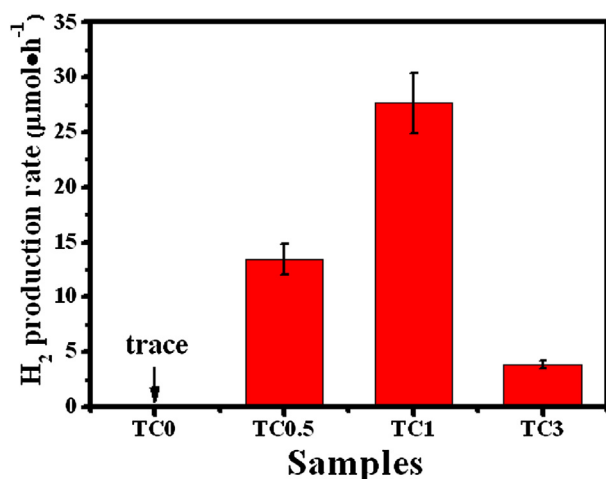
Fig. 8. Comparison of the photocatalytic H_2-production activities for TiO_2 and Co_3O_4 composite samples TCx.
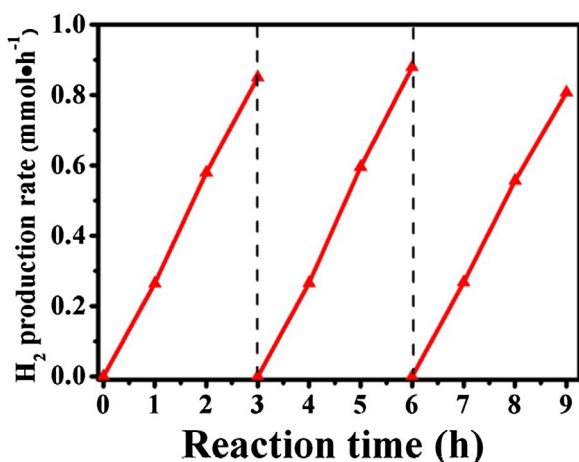

Fig. 9. Cycling curves of H_2-production activity for sample TCP.

NPs may shield the incident light and act as charge recombination centres.

Remarkably, when both the optimized amount of Pt (1 wt%) and Co_3O_4 (1 wt%) cocatalysts are simultaneously located on the corresponding facets, the H_2-production activity of TCP composite photocatalyst can be further enhanced. It can be seen that the H_2-production activity of sample TCP reaches 264 μmol h^{-1} (the corresponding quantum efficiency is 11.3% at 365 nm), which exceeds the rate of TiO_2 loaded with Pt or Co_3O_4 alone as cocatalyst by 1.8 and 9.4 times, respectively. Besides, the H_2-production activity of TCP is higher than the sum of TC1 and TP1, suggesting the presence of the synergetic effect of Pt and Co_3O_4 dual-cocatalysts. Moreover, this composite photocatalyst remains stable after photocatalytic reaction for 9 h (Fig. 9). These results indicate that

the co-loading of Pt and Co_3O_4 cocatalysts is an efficient way to enhance the H_2-production activity of TiO_2 and the prepared TiO_2-Co_3O_4-Pt composite is a highly efficient and robust photocatalyst.

In order to further investigate the influence of the distribution of Pt and Co_3O_4 cocatalysts on the photocatalytic H_2-production activity of the prepared composites, the H_2-production activity of TCP(r) and TC(r)P samples was tested as comparisons (Fig. 6). For sample TCP(r), Co_3O_4 was selectively loaded on {001} facets of TiO_2 by photodeposition method while Pt was randomly loaded on {001} and {101} facets of TiO_2 through NaBH$_4$ reduction method. Similarly, for sample TC(r)P, Pt was selectively loaded on {101} facets of TiO_2 by photodepostion method, while Co_3O_4 was randomly loaded on {101} and {001} facets of TiO_2 by impregnation-calcination method. The selective and random deposition procedures of Pt WRC and Co_3O_4 WOC are illustrated in Figs. 10–12 . During the selective photodeposition of Co_3O_4 and Pt cocatalyst (Fig. 10), due to the surface heterojunction between the two exposed facets, the photogenerated electrons and holes migrate to {101} and {001} facets, respectively [30]. Consequently, Pt^{4+} can only be reduced effectively by the electrons on the {101} facets to form Pt NPs. Contrarily, partial Co^{2+} can be oxidized to Co^{3+} by the holes accumulated on the {001} facets and the Co_3O_4 NPs are finally deposited on the {001} facets of TiO_2. This is easily understood because the conduction band (CB) potential of TiO_2 (−0.42 eV vs. NHE, pH = 7) is more negative than the reduction potential of $PtCl_6^{2-}$/Pt (0.32 eV vs. NHE, pH = 7), and the valence band (VB) potential of TiO_2 (2.78 eV vs. NHE, pH = 7) is more positive than the oxidation potential of Co^{2+}/Co^{3+} (0.7 eV vs. NHE, pH = 7) [62,63]. Hence, the surface Pt cocatalyst can be selectively reduced and deposited on {101} facets as the reduction active site, while Co_3O_4 cocatalyst is selectively oxidized and deposited on {001} facets as the oxidation active site, and the photogenereated charge carriers from TiO_2 are most likely to migrate to these photocatalytic active sites to participate in photocatalytic reactions. However, for TCP(r) sample (Fig. 11), $PtCl_6^{2-}$ is uniformly dispersed in an aqueous solution and rapidly reduced by adding NaBH$_4$ into the solution, forming small Pt NPs. These small Pt NPs then adsorb on all facets of anatase TiO_2 nanosheets. Besides, for TC(r)P sample (Fig. 12), after water evaporation, $Co(NO_3)_2$ was uniformly deposited on the surface of whole TiO_2 nanosheets. Finally, $Co(NO_3)_2$ was completely decomposed and oxidized into Co_3O_4 at 350 °C. Thus, these Co_3O_4 NPs were randomly attached on {101} and {001} facets of TiO_2 nanosheets. Therefore, It is not surprising that the photocatalytic activities of TCP(r) and TC(r)P samples greatly decrease comparing with TCP sample because its Pt and Co_3O_4 NPs were selectively deposited on {101} and {001} facets and used as reduction and oxidation cocatalysts, respectively. This also implies that the recombination center easily formed when Pt and Co_3O_4 NPs were simultaneously deposited on the same facets due to their contact each other.
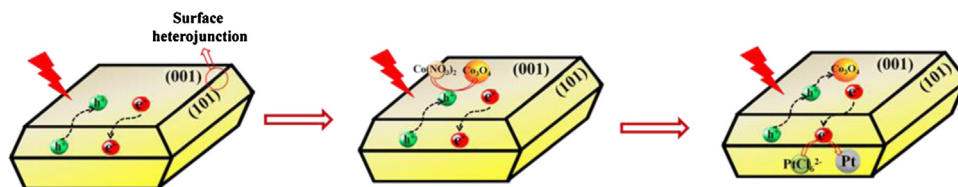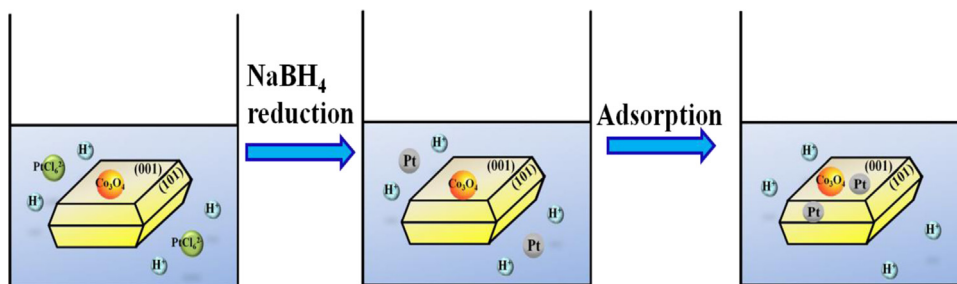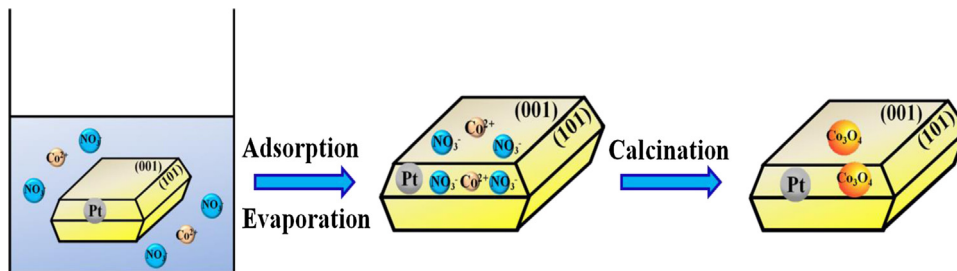

**Fig. 10.** Schematic illustration of TCP sample for the charge separation and selective photodeposition of Co_3O_4 and Pt cocatalysts on {001} and {101} facets, respectively. The photogenerated holes transfer from {101} to {001} facets, on which Co^{2+} was oxidized into Co_3O_4. The photogenerated electrons transfer from {001} to {101} facets, on which $PtCl_6^{2-}$ was reduced into Pt.

Fig. 11. Schematic illustration for preparation of sample TCP(r) using the NaBH$_4$ reduction process. Co$_3$O$_4$ NPs were firstly and selectively photodeposited on {001} facets, then, Pt NPs were randomly deposited on {101} and {001} facets.

Fig. 12. Schematic illustration for preparation of sample TC(r)P using the impregnation-calcination process. Pt NPs were firstly and selectively photodeposited on {101} facets, then, Co$_3$O$_4$ NPs were randomly attached on {101} and {001} facets.
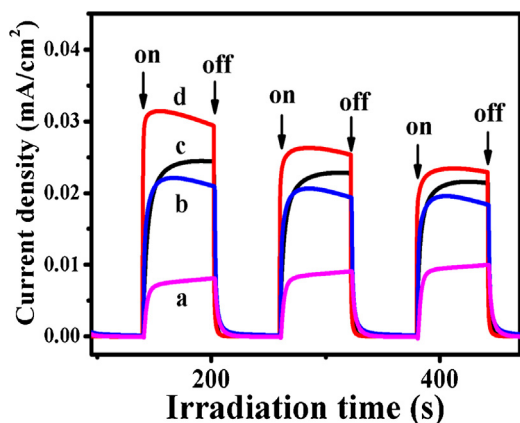
Fig. 13. Transient photocurrent responses of T (a), TC1 (b), TP1 (c), TCP (d) samples.

3.6. Transient photocurrent analysis

Fig. 13 shows the transient photocurrent responses of the samples recorded with several on-off cycles under UV light irradiation. It can be seen that all the samples show an immediate rise in the photocurrent response when the light was on. Contrarily, the photocurrent rapidly decreases to zero when the light was turned off. The on-off cycles of photocurrent are reproducible, which indicates that the photogenerated electrons are transferred to the back contact across the samples to form photocurrent under light irradiation [64]. Furthermore, the photocurrent density of TC1 and TP1 is higher than that of the pristine TiO$_2$. Also, the TCP sample shows the highest photocurrent density, indicating a noticeable improvement of charge separation efficiency by the introduction of Co$_3$O$_4$ and Pt dual cocatalysts [65].

3.7. Photocatalytic mechanism

From what has been observed and discussed above, the high photocatalytic H$_2$-production activity of TCP can be explained by the scheme shown in Fig. 14. During light irradiation, the VB electrons of anatase TiO$_2$ are excited to the CB, while holes remain in VB. Due to the presence of surface heterojunction, the photogenerated electrons and holes migrate to {101} and {001} facets, respectively. On the {101} facets, the accumulated electrons will further transfer to Pt NPs due to its large work function and low Fermi level. Then Pt NPs act as the reduction active sites, in which the electrons can reduce H$_2$O to produce hydrogen molecule [66,67]. On the contrary, on the {001} facets, when p-type Co$_3$O$_4$ NPs were closely attached on the hole-rich {001} facets of n-type TiO$_2$ due to high-temperature calcination, the p-n junction can be formed at the interface of TiO$_2$ and Co$_3$O$_4$. Thus the inner electric field in *p-n* junction can efficiently accelerate the transport of holes into Co$_3$O$_4$ NPs, in which the assembled holes are consumed by the sacrificial reagents or water oxidation. This indicates that the notable synergetic effect was caused by the surface heterojunction and the dual-cocatalysts. Therefore, the TCP composite photocatalyst shows a great enhanced photocatalytic H$_2$-production activity comparing with samples TP and TC with only Pt or Co$_3$O$_4$ alone as a cocatalyst. However, for sample TCP(r), Co$_3$O$_4$ NPs were selectively loaded on {001} facets while Pt NPs were randomly loaded on both {101} and {001} facets. As a result, the Pt NPs loaded on {001} facets will directly contact with Co$_3$O$_4$ NPs and holes on {001} facets, thus inhibiting the transfer of electrons from {001} to {101} facets, and becoming a recombination centre of photogenerated electrons and holes. Therefore, it is easy to understand that the TCP(r) sample shows lower activity than TCP sample. Further, for sample TC(r)P, Pt was selectively deposited on {101} facets while Co$_3$O$_4$ was randomly attached by impregnation-calcination method. In this case, the Co$_3$O$_4$ attached on {101} facets will directly contact with Pt NPs and electrons on {101} facets, thus inhibiting the transfer of holes from {101} to {001} facets and becoming an electron-hole recombination center. Therefore, not surprising, the TC(r)P sam-
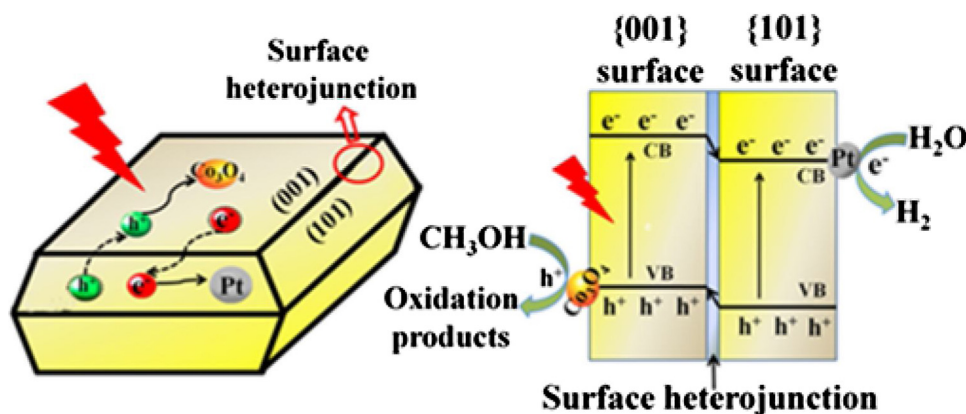
Fig. 14. Schematic illustration for the synergetic effect of the surface heterojunction between {101} and {001} facets and the selective deposition of dual-cocatalysts on {101} and {001} facets of TiO_2. The former is beneficial for the spatial transfer and separation of photogenerated charged carriers and the latter beneficial for occurrence of reduction and oxidation reactions on different regions.

ple also exhibits a lower H_2-production activity than TCP sample, and even lower than TC1 and TP1 samples. These results for the first time clearly show that not only the suitable contents of Pt and Co_3O_4 but also the loading locations of the cocatalysts are crucial for improving the photocatalytic H_2-production activity of TiO_2.

4. Conclusions

In summary, anatase TiO_2 nanosheets co-deposited with Co_3O_4 WOC on {001} facets and Pt WRC on {101} facets were prepared, which exhibits higher photocatalytic H_2-production rate than TiO_2 nanosheet deposited with Co_3O_4 or Pt single cocatalyst by 9.4 and 1.8 times, respectively. The enhanced photocatalytic H_2-production activity of the TiO_2-Co_3O_4-Pt composite photocatalyst can be attributed to the synergetic effect of surface heterojunction between {001} and {101} facets of TiO_2 nanosheets as well as the selective deposition of Co_3O_4 WOC and Pt WRC dual-cocatalysts, locating at {001} and {101} facets, respectively. The former can greatly suppress the recombination of charge carriers and the latter can provide more catalytic active sites for photocatalytic reactions. The results show that not only the combination of Co_3O_4 and Pt cocatalysts but also the loading locations and distributions of the cocatalysts are very crucial for the enhancement of high photocatalytic H_2-production activity. This work shows a simple route for the selective deposition of suitable cocatalysts onto the different facets of TiO_2, which provides new insight for the fabrication of highly efficient photocatalysts with dual-cocatalysts.

References

[1] F. Sordello, C. Minero, Appl. Catal. B 163 (2015) 452–458.
[2] Q.J. Xiang, B. Cheng, J.G. Yu, Angew. Chem. Int. Ed. 54 (2015) 11350–11366.
[3] X. Li, J.G. Yu, J.X. Low, Y.P. Fang, J. Xiao, X.B. Chen, J. Mater. Chem. A. 3 (2015) 2485–2534.
[4] A. Kudo, Y. Miseki, Chem. Soc. Rev. 38 (2009) 253–278.
[5] Q. Li, X. Li, S. Wageh, A.A. Al-Ghamdi, J.G. Yu, Adv. Energy Mater. 5 (2015) 1500010.
[6] C. Liu, L. Wang, Y. Tang, S. Luo, Y. Liu, S. Zhang, Y. Zeng, Y. Xu, Appl. Catal. B 164 (2015) 1–9.
[7] C. Wang, Q.Q. Hu, J.Q. Huang, C. Zhu, Z.H. Deng, H.L. Shi, L. Wu, Z.G. Liu, Y.G. Cao, Appl. Surf. Sci. 292 (2014) 161–164.
[8] Z. Zhang, S.W. Cao, Y. Liao, C. Xue, Appl. Catal. B 162 (2015) 204–209.
[9] A. Moya, A. Cherevan, S. Marchesan, P. Gebhardt, M. Prato, D. Eder, J.J. Vilatela, Appl. Catal. B 179 (2015) 574–582.
[10] Q.L. Xu, J.G. Yu, J. Zhang, J.F. Zhang, G. Liu, Chem. Commun. 51 (2015) 7950–7953.
[11] T. Sun, E.Z. Liu, X.H. Liang, X.Y. Hu, J. Fan, Appl. Surf. Sci. 347 (2015) 696–705.
[12] D.Y.C. Leung, X.L. Fu, C.F. Wang, M. Ni, M.K.H. Leung, X.X. Wang, X.Z. Fu, ChemSusChem 3 (2010) 681–694.
[13] R. Dholam, N. Patel, M. Adami, A. Miotello, Int. J. Hydrogen Energy 34 (2009) 5337–5346.
[14] H. Park, W. Choi, M.R. Hoffmann, J. Mater. Chem. 18 (2008) 2379–2385.
[15] J.S. Jang, S.H. Choi, H.G. Kim, J.S. Lee, J. Phys. Chem. C 112 (2008) 17200–17205.
[16] C.H. Wang, X.T. Zhang, Y.C. Liu, Appl. Surf. Sci. 358 (2015) 28–45.
[17] H.G. Yang, C.H. Sun, S.Z. Qiao, J. Zou, G. Liu, S.C. Smith, H.M. Cheng, G.Q. Lu, Nature 453 (2008) 638–642.
[18] G. Liu, H.G. Yang, J. Pan, Y.Q. Yang, G.Q. Lu, H.M. Cheng, Chem. Rev. 114 (2014) 9559–9612.
[19] J.G. Yu, L.F. Qi, M. Jaroniec, J. Phys. Chem. C 114 (2010) 13118–13125.
[20] G. Liu, C.H. Sun, H.G. Yang, S.C. Smith, L.Z. Wang, G.Q. Lu, H.M. Cheng, Chem. Commun. 46 (2009) 755–757.
[21] C.Z. Wen, J.Z. Zhou, H.B. Jiang, Q.H. Hu, S.Z. Qiao, H.G. Yang, Chem. Commun. 47 (2011) 4400–4402.
[22] X.Y. Ma, Z.G. Chen, S.B. Hartono, H.B. Jiang, J. Zou, S.Z. Qiao, H.G. Yang, Chem. Commun. 46 (2010) 6608–6610.
[23] Y.Q. Dai, C.M. Cobley, J. Zeng, Y.M. Sun, Y.N. Xia, Nano Lett. 9 (2009) 2455–2459.
[24] H.G. Yang, G. Liu, S.Z. Qiao, C.H. Sun, Y.G. Jin, S.C. Smith, J. Zou, H.M. Cheng, G.Q. Lu, J. Am. Chem. Soc. 131 (2009) 4078–4083.
[25] X.G. Han, Q. Kuang, M.S. Jin, Z.X. Xie, L.S. Zheng, J. Am. Chem. Soc. 131 (2009) 3152–3153.
[26] L. Ren, Y.Z. Li, J.T. Hou, J.L. Bai, M.Y. Mao, M. Zeng, X.J. Zhao, N. Li, Appl. Catal. B 181 (2016) 625–634.
[27] H.M. Zhang, P. Liu, F. Li, H.W. Liu, Y. Wang, S.Q. Zhang, M.X. Guo, H.M. Cheng, H.J. Zhao, J. Chem. Eur. 17 (2011) 5949–5957.
[28] N. Roy, Y. Sohn, D. Pradhan, ACS Nano 7 (2013) 2532–2540.
[29] Z.K. Zheng, B.B. Huang, J.B. Lu, X.Y. Qin, X.Y. Zhang, Y. Dai, Chem. Eur. J. 17 (2011) 15032–15038.
[30] T. Ohno, K. Sarukawa, M. Matsumura, New J. Chem. 26 (2002) 1167–1170.
[31] J.G. Yu, J.X. Low, W. Xiao, P. Zhou, M. Jaroniec, J. Am. Chem. Soc. 136 (2014) 8839–8842.
[32] T.R. Gordon, M. Cargnello, T. Paik, F. Mangolini, R.T. Weber, P. Fornasiero, C.B. Murray, J. Am. Chem. Soc. 134 (2012) 6751–6761.
[33] J.H. Yang, D. Wang, H.X. Han, C. Li, Acc. Chem. Res. 46 (2013) 1900–1909.
[34] J.R. Ran, J. Zhang, J.G. Yu, M. Jaroniec, S.Z. Qiao, Chem. Soc. Rev. 43 (2014) 7787–7812.
[35] Y. Xu, R. Xu, Appl. Surf. Sci. 351 (2015) 779–793.
[36] J. Puskelova, R. Michal, M. Caplovicova, M. Antoniadou, L. Caplovic, G. Plesch, P. Lianos, Appl. Surf. Sci. 305 (2014) 665–669.
[37] J.G. Yu, Y. Hai, M. Jaroniec, J. Colloid Interface Sci. 357 (2011) 223–228.
[38] H.G. Yu, P. Xiao, P. Wang, J.G. Yu, Appl. Catal. B 193 (2016) 217–225.
[39] J.Q. Wen, X. Li, W. Liu, Y.P. Fang, J. Xie, Y.H. Xu, Chin. J. Catal. 36 (2015) 2049–2070.
[40] D. Wang, R.G. Li, J. Zhu, J.Y. Shi, J.F. Han, X. Zong, C. Li, J. Phys. Chem. C 116 (2012) 5082–5089.
[41] B.J. Ma, F.Y. Wen, H.F. Jiang, J.H. Yang, P.L. Ying, C. Li, Catal. Lett. 134 (2010) 78–86.

[42] K. Maeda, A. Xiong, T. Yoshinaga, T. Ikeda, N. Sakamoto, M. Hisatomi, M. Takashima, D.L. Lu, M. Kanehara, T. Setoyama, T. Teranishi, K. Domen, Angew. Chem. Int. Ed. 49 (2010) 4096–4099.
[43] H.J. Yan, J.H. Yang, G.J. Ma, G.P. Wu, X. Zong, Z.B. Lei, J.Y. Shi, C. Li, J. Catal. 266 (2009) 165–168.
[44] B. Cao, G.S. Li, H.X. Li, Appl. Catal. B 194 (2016) 42–49.
[45] D.A. Wang, T. Hisatomi, T. Takata, C.S. Pan, M. Katayama, J. Kubota, K. Domen, Angew. Chem. Int. Ed. 52 (2013) 11252–11256.
[46] R.G. Li, H.X. Han, F.X. Zhang, D. Wang, C. Li, Energy Environ. Sci. 7 (2014) 1369–1376.
[47] L.H. Nie, J.G. Yu, X.Y. Li, B. Cheng, G. Liu, M. Jaroniec, Environ. Sci. Technol. 47 (2013) 2777–2783.
[48] K.S.W. Sing, D.H. Everett, R.A.W. Haul, L. Moscou, R.A. Poerotti, J. Rouquerol, T. Siemieniewska, Pure Appl. Chem. 57 (1985) 603–619.
[49] T.S. Markova, O.V. Yanush, Russ. J. Appl. Chem. 5 (2008) 779–785.
[50] A.H. Lv, C. Hu, Y.L. Nie, J.H. Qu, Appl. Catal. B 117 (2012) 246–252.
[51] Z.Z. Zhu, G.Z. Lu, Z.G. Zhang, Y. Guo, Y.L. Guo, Y.Q. Wang, ACS Catal. 3 (2013) 1154–1164.
[52] L.H. Nie, P. Zhou, J.G. Yu, M. Jaroniec, J. Mol. Catal. A 390 (2014) 7–13.
[53] Z.Z. Zheng, X.H. Wang, J. Liu, J.H. Xiao, Z.Y. Hu, Appl. Surf. Sci. 309 (2014) 144–152.
[54] H.B. Michaelson, J. Appl. Phys. 48 (1977) 4729–4733.
[55] J.G. Yu, Y. Hai, B. Cheng, J. Phys. Chem. C 115 (2011) 4953–4958.
[56] J. Zhang, L.F. Qi, J.R. Ran, J.G. Yu, S.Z. Qiao, Adv. Energy Mater. 4 (2014) 1301925.
[57] R.G. Li, Z. Chen, W. Zhao, F.X. Zhang, K. Maeda, B.K. Huang, S. Shen, K. Domen, C. Li, J. Phys. Chem. C 117 (2013) 376–382.
[58] F.X. Zhang, A. Yamakata, K. Maeda, Y. Moriya, T. Takata, J. Kubota, K. Teshima, S. Qishi, K. Domen, J. Am. Chem. Soc. 134 (2012) 8348–8351.
[59] Z.P. Yan, H.T. Wu, A.L. Han, X.X. Yu, P.W. Du, Int. J. Hydrogen Energy 39 (2014) 13353–13360.
[60] J.L. Yuan, J.Q. Wen, Q.Z. Gao, S.C. Chen, J.M. Li, X. Li, Y.P. Fang, Dalton Trans. 44 (2015) 1680–1689.
[61] O. Yehezkeli, D.R.B.D. Oliveira, J.N. Cha, Small 11 (2015) 668–674.
[62] X. Li, J.Q. Wen, J.X. Low, Y.P. Fang, J.G. Yu, Sci. China Mater. 57 (2014) 1–31.
[63] E.M.P. Steinmiller, K.S. Choi, Proc. Natl. Acad. Sci. U. S. A. 106 (2009) 20633–20636.
[64] J. Zhang, S.Z. Qiao, L.F. Qi, J.G. Yu, Phys. Chem. Chem. Phys. 15 (2013) 12088–12094.
[65] Q.J. Xiang, J.G. Yu, M. Jaroniec, J. Am. Chem. Soc. 134 (2012) 6575–6578.
[66] C. Liu, X.G. Han, S.F. Xie, X. Kuang, M.S. Jin, Z.X. Xie, L.S. Zheng, Chem. Asian J. 8 (2013) 282–289.
[67] M.S. Akple, J. Low, S. Wageh, A.A. Al-Ghamdi, J. Yu, J. Zhang, Appl. Surf. Sci. 358 (2015) 192–196.